Article

Monitoring Soil Moisture Drought over Northern High Latitudes from Space

Jostein Blyverket[1,2]*, Paul D. Hamer[1], P. Schneider[1], Clément Albergel[3], William A. Lahoz[1]

1 Norwegian Institute for Air Research NILU, Instituttveien 18, 2007 Kjeller, Norway; jb@nilu.no
2 University of Bergen UiB, Geofysisk institutt Allegaten 70, 5020 Bergen, Norway.
3 CNRM - Université de Toulouse, Météo-France, CNRS, Toulouse, France.
* Correspondence: jb@nilu.no

Abstract: Mapping drought from space using, e.g., surface soil moisture (SSM), has become viable in the last decade. However, state of the art SSM retrieval products suffer from very poor coverage over northern latitudes. In this study, we propose an innovative drought indicator with a wider spatial and temporal coverage than that obtained from satellite SSM retrievals. We evaluate passive microwave brightness temperature observations from the Soil Moisture and Ocean Salinity (SMOS) satellite as a surrogate drought metric, and introduce a Standardized Brightness Temperature Index (STBI). The STBI is validated against drought indices from a land surface data assimilation system (LDAS-Monde), two satellite dervied SSM indices and a standardized precipitation index. Finally, we evaluate the STBI against the before mentioned drought indices in a case study of the 2018 Nordic drought. The STBI is found to be superior to the drought index created from satellite derived SSM in both spatial and temporal coverage over the Nordic region. Our results indicate that when compared to drought indices from precipitation data and a land data assimilation system, the STBI is able to capture the 2018 drought onset, severity and extent. Thus, the STBI index could provide additional information for drought monitoring in regions where the SSM retrieval problem is difficult.

Keywords: SMOS; Drought Index; Summer 2018 drought

---

1. Introduction

Droughts cost society billions of dollars every year, estimates from the World Meteorological Organization WMO show that in the European Union alone droughts cost around 6.2 billion USD per year [1]. It is therefore important to implement tools that can monitor and warn about drought conditions, in order to mitigate and prevent losses from droughts [2,3]. Such tools will provide policy and decision makers with a quantitative measure of drought characteristics, allowing them to act upon scientifically based data. Drought indices from different sources, i.e., satellite platforms, models and in-situ observations are crucial components of drought monitoring tools. By utilizing information (and creating drought indices) from multiple sources one avoids relying too much on just one source of information and the possible failure of this source to capture the drought.

In the spring and early summer of 2018 severe drought conditions developed over the Nordic countries, Norway, Sweden, Finland and Denmark [4,5]. The drought conditions caused wildfires, decreased crop yield and increased crop failure, which resulted in large private and governmental economic losses. In Norway alone the preliminary payout from the government to farmers (3 January 2019) have reached 187 million USD, compared to 4.9 million USD per year on average for the 2008-2017 period [6]. Late winter and early spring precipitation deficit lead to a decrease in soil moisture, which did not recover until late August and September [7]. For example, the rainfall for May to July in Lund, Sweden, was only about half of the previous low record, with observations dating back to 1748 [5]. Droughts are rare in the Nordic countries, and regional monitoring capabilities and preventive measures were lacking, likely increasing the negative impacts of the drought. Recent studies have found that climate change is likely to exacerbate droughts [8]; as a result, the drought will set in

Preprints (www.preprints.org) | NOT PEER-REVIEWED | Posted: 1 April 2019 doi:10.20944/preprints201904.0009.v1

Peer-reviewed version available at Remote Sens. 2019, 11, 1200; doi:10.3390/rs11101200

quicker and be more intense [9]. Although the Nordic region is projected to get wetter conditions on average under climate change [8], droughts might still occur, and thus a way of monitoring and mapping droughts over the northern regions is much needed. One way of doing this is by satellite remote sensing [10–12], as satellites could provide near-real-time observations covering large regions within a relative short amount of time.

Satellite retrieval of surface soil moisture over northern latitudes is difficult because of snow cover, high open water fraction, steep topography and dense boreal vegetation that affect the microwave emissions from the soil [13]. This eventually results in large regions where the retrievals are missing (masked), and hence the spatial and temporal coverage of satellite derived soil moisture over this region is poor. Although the inversion from brightness temperature to soil moisture might be ill posed, the microwave signal carries information about water content in the vegetation (VWC) and soil system [14]. Thus, anomalies in the water content of the vegetation-soil system will be reflected in anomalies in the passive microwave brightness temperature. In this paper we argue that when studying hydrological extremes, such as drought, we can omit the satellite soil moisture retrieval problem over northern latitudes and look at the raw radiances (microwave brightness temperature, Tb) instead. The rationale is that the Tb is a convolution of soil moisture and VWC [11,15], hence it can be used to map drought (onset, extent and recovery) from space over northern latitudes, a region where soil moisture retrieval products have large spatial and temporal gaps. In this work we introduce the Standardized Brightness Temperature Index (STBI) for drought monitoring over northern high latitudes.

This paper is divided into four parts, Sec. 1 introduces the paper, in Sec. 2 we present the remote sensing, precipitation and modelling data; we also introduce the methods for the computation of the standardized drought indices. In Sec. 3.1 we evaluate the temporal dynamics of the STBI index using the Standardized Precipitation Index (SPI) from the gridded E-OBS in-situ rainfall dataset, and two Standardized Soil moisture Indices (SSI), one from the National Centre for Meteorological Research (CNRS) Météo-France Land Data Assimilation System Monde (LDAS-Monde), and one from the European Space Agency Climate Change Initiative (ESA CCI) satellite derived soil moisture product. In Sec. 3.2 a case study of the summer 2018 Nordic drought is used to evaluate the STBI drought monitoring capabilities. Finally, in Sec. 4 we present our conclusions.

2. Data and Methods

2.1. Remote Sensing Data

Launched in November 2009 by the European Space Agency (ESA), the Soil Moisture and Ocean Salinity (SMOS) satellite is dedicated to measure passive microwave emissions in the L-band from the Earth surface [13]. Here we use the SMOS Level-2 SMUDP2 version 650 reprocessed data (2010-2017) and the operational (April, May, June, July, August and September 2018) brightness temperature data with horizontal polarization (Tb_H). From this product we also extract the Level-2 soil moisture product, used to compute the SMOS standardized soil moisture index. The data are obtained from the ESA SMOS dissemination service [16]. The SMOS retrieval algorithm simultaneously retrieves soil moisture and vegetation optical depth by using information from mutli-angle observations of Tb at horizontal and vertical polarization. The SMOS retrieval is done by minimizing the difference between the satellite observed and model simulated Tb, using the L-band Microwave Emission of the Biosphere model (L-MEB) [13,17]. The horizontal polarization is chosen because other studies show that it is more sensitive to surface soil moisture than the vertical polarization [18]. However, we found little difference when applying the vertical polarization instead of the horizontal polarization in the computation of the microwave drought index, we therefore only show results for the horizontal polarization.

At L-band the Tb_H is sensitive to soil moisture in the upper $0-5$ cm of the soil [19]. A limitation of the satellite derived drought index is the sensing depth, so we are unable to quantify the amount

Preprints (www.preprints.org) | NOT PEER-REVIEWED | Posted: 1 April 2019 doi:10.20944/preprints201904.0009.v1

Peer-reviewed version available at Remote Sens. 2019, 11, 1200; doi:10.3390/rs11101200

of water in the root-zone. The 2018 drought set in early in the growing season, meaning that plants were more reliant on surface zone soil moisture than root-zone soil moisture. Thus, the limited sensing depth should not constrain this study too much [12].

The microwave emissions are larger for a dry soil than for a wet soil [20], and the satellite observed Tb_H also depends on the effective soil and canopy temperature [21]. In addition the Tb_H is linked to the VWC; an increase in VWC leads to an increase in the observed brightness temperature [15]. Effectively, this means that under dry vegetation conditions a larger fraction of the observed brightness temperature over vegetated areas will come from the soil, as the vegetation masking of the signal will be smaller than under wet conditions.

The SMOS Level-2 swath data are gridded to the Equal Area Scalable Earth (EASE) version 2.0 36 km grid using a nearest neighbour method; this is done to avoid smoothing from an interpolation scheme. The SMOS data are extracted for the period 1 July 2010 until 1 October 2018 (April, May and June 2010 are not utilized, following [22]). We only use the morning overpass to ensure that the land-atmosphere system is as close as possible to thermal equilibrium. The Tb_H data are screened for values outside a range of $100 - 320$ K [22]. Other than that we do not do any detailed quality control, because part of this work is to see if the SMOS Tb_H data contains drought information regardless of grid-cell properties. Monthly Tb_H climatology is computed by averaging the ~ 6 a.m. overpasses; this is done for April, May, June, July, August and September from 2010 (except April, May and June 2010) until 2018. Only grid-cells with nine years of data are included in the climatology, except for April, May and June where we use eight years of data.

The monthly satellite derived soil moisture from the ESA CCI soil moisture project is extracted from the Copernicus Climate Change Service (C3S) [23,24]. We utilize the COMBINED product, which is a combination of soil moisture retrievals from passive and active satellite sensors, such as METOP-A, METOP-B, AMSR2 and SMOS [25]. The COMBINED product is posted on a 0.25° regular longitude/latitude grid. The dataset spans from 1979 until present; however, because of spatial and temporal gaps in the product, we only use data from April 2010 until October 2018 (i.e., the same time-period as the SMOS-L2 product). This also ensures that the climatologies for the standardized indices are computed over the same time-period.

2.2. Precipitation Data

In this study, we use the E-OBS version 17.0 precipitation dataset, which corresponds of in-situ rain gauge data posted on a 0.25° grid [26]. Data for June, July, August and September 2018 are not included in v17.0 and were therefore downloaded separately. The E-OBS dataset spans from 1st January 1950 until 1st October 2018. The one month Standardized Precipitation Index (SPI-1) is computed to create a measure of drought, which is independent from the STBI (Tb_H) data. Accumulated total precipitation for individual months is computed by summarizing daily precipitation (mm/day) for each month separately from 1950 until October 2018.

2.3. LDAS-Monde Soil Moisture Data

Analysis soil moisture data are from the Land Data Assimilation System Monde (LDAS-Monde) [27], which has recently been applied to monitor and forecast the impact of the 2018 summer drought on vegetation over central Europe [28]. We run the LDAS-Monde system over the Nordic region using ERA-5 reanalysis atmospheric forcing data and the ISBA (Interaction between Soil Biosphere and Atmosphere) land surface model [29,30] within the SURFEX v.8.1 (SURFace EXternalisée) modelling framework [31]. Surface soil moisture derived from the METOP satellite platforms and Leaf Area Index (LAI) observation data from the Copernicus Global Land (CGL) service are assimilated into the LDAS-Monde system using a simplified extended Kalman Filter (SEKF) [32–35]. The LDAS-Monde system is setup at a 0.25° regular longitude/latitude grid. Monthly means for the 2010 to 2018 period are created from the 6 a.m. surface soil moisture model data; this is done to correspond as closely as possible with the SMOS overpass time and the Tb_H observation time.

Preprints (www.preprints.org) | NOT PEER-REVIEWED | Posted: 1 April 2019 doi:10.20944/preprints201904.0009.v1

Peer-reviewed version available at Remote Sens. 2019, 11, 1200; doi:10.3390/rs11101200

2.4. Computation of the Standardized microwave Brightness Temperature Index (STBI)

In this section we introduce the new Standardized microwave Brightness Temperature Index (STBI). Which to the best of our knowledge has not been utilized for drought monitoring before. In this work the STBI is based on SMOS data. However, it can also be estimated based on data from other L-band satellites, for example, the Soil Moisture Active Passive (SMAP) NASA mission [19]. The STBI_SMOS is computed assuming that the $\mathrm{Tb_H}$ in each grid-cell follows a Gaussian probability distribution. This assumption is tested using the Shapiro-Wilk test, where the null hypothesis is that our sample comes from a normally distributed population. To fit the Gaussian distribution to the $\mathrm{Tb_H}$ data we use the maximum likelihood method; this is done separately for each grid-cell. We then compute the PDF of monthly $\mathrm{Tb_H}$ data, for each summer month. By integrating over $(0, \mathrm{Tb}_\mathrm{H}^i)$ we find the probability of a given Tb_H^i value. This value is then converted to a standardized index using:

$$\mathrm{STBI} = \Phi^{-1}(p(\mathrm{Tb}_\mathrm{H}^i)), \tag{1}$$

where Φ^{-1} is the inverse standard normal distribution with zero mean and a standard deviation of one. The standardization is based on an approximation detailed in [36].

2.5. Computation of the Standardized Soil moisture Index

For comparison to the STBI_SMOS index we compute three standardized soil moisture indices (SSI_ESA_CCI, SSI_LDAS and SSI_SMOS), they are computed by assuming a Beta distribution for the underlying soil moisture data [12,37]. The Beta probability distribution is given as:

$$f(\theta) = \frac{\theta^{\alpha-1}(1-\theta)^{\beta-1}}{B(\alpha,\beta)}, \tag{2}$$

where $B = \frac{\Gamma(\alpha)\Gamma(\beta)}{\Gamma(\alpha+\beta)}$, θ is the volumetric soil moisture content, α and β are shape parameters. First we find the upper and lower limit on soil moisture for each individual grid-cell and month. We assume that the first/last 10 % of the sorted soil moisture values are linearly related to their empirical distribution function. After the computation of the upper and lower soil moisture values, we find the Beta distribution shape parameters (α and β) using the maximum likelihood method. We then use Eq. 2 to compute the probability density function (PDF) of monthly soil moisture, for each summer month. By integrating over $(0, \theta)$ we find the probability of a θ value. This value is then used in Eq. 1, to find the standardized index (SSI). Negative/positive SSI values are below/above the average climatology of soil moisture and indicate a dry/wet period.

2.6. Computation of the Standardized Precipitation Index

For the sake of comparison with the land surface drought indices (STBI and SSI) we also compute a Standardized Precipitation Index (SPI). The SPI is frequently used in studies and monitoring of meteorological drought, it is used to characterize droughts at time-scales of 1 to 36 months. On shorter time-scales the SPI is found to be closely related to soil moisture drought, while at longer time-scales it is more closely related to groundwater drought [12]. We therefore chose to compute the one-month SPI (SPI-1). The general interpretation of the SPI is that it expresses the number of standard deviations the anomaly deviates from the long-term mean. In the computation of the SPI-1 we use a non-parametric standardization approach. The empirical probabilities of the E-OBS precipitation data are computed for each individual grid-cell, using the empirical Gringorten plotting position [36,38].

$$p(\mathrm{rainf}) = \frac{i-0.44}{n+0.12}, \tag{3}$$

where i is the rank of the precipitation data from the smallest value, and n is the sample size. The constants 0.44 and 0.12 are unique for this plotting position. An empirical relationship is applied

Preprints (www.preprints.org) | NOT PEER-REVIEWED | Posted: 1 April 2019 doi:10.20944/preprints201904.0009.v1

Peer-reviewed version available at *Remote Sens.* **2019**, *11*, 1200; doi:10.3390/rs11101200

because the length of the dataset allows this (69 years) and we avoid assuming one constant parametric distribution function for each grid-cell. The empirical probabilities are converted to a standardized index using Eq. 1.

Negative or positive SPI-1 values indicate a below (dry) or above (wet) average climatology for the precipitation or soil moisture, respectively. For the STBI_SMOS a high and therefore warm Tb_H reflects drier conditions, while a low and cold Tb_H reflects wetter conditions. We therefore multiply the STBI_SMOS with -1, for the sake of comparison with the SPI-1 and SSI.

3. Results and Discussion

3.1. Evaluation of the proposed Standardized microwave Brightness Temperature Index

3.1.1. Tb_H probability distribution

The Tb_H distribution for each summer month is assumed to follow a Gaussian distribution. This assumption is tested using the Shapiro-Wilk test on the boreal summer (June, July and August) data. The Shapiro-Wilk test looks at the correlation between the data and the Gaussian quantile. This test only checks if the data were drawn from a normal distribution, it does not check what the parameters of that distribution might be [39]. Our null-hypothesis is that the data are normally distributed. If the p-value is smaller than a chosen α value then the null-hypothesis is rejected and there is evidence that the data are not normally distributed. If the p-value is larger than the chosen α value we cannot reject the null-hypothesis that the data are normally distributed, hence the data are likely normally distributed. Here we choose $\alpha = 0.05$. In Fig. 1 a) grid-cells in dark blue show where the null-hypothesis was not rejected, light blue grid-cells show where the null-hypothesis was rejected. White regions over land show where we had less than eight years of data for the Shapiro-Wilk test, these regions are excluded in the calculation. The Gaussian fit to the Tb_H for June (red), July (blue) and August (black) are shown

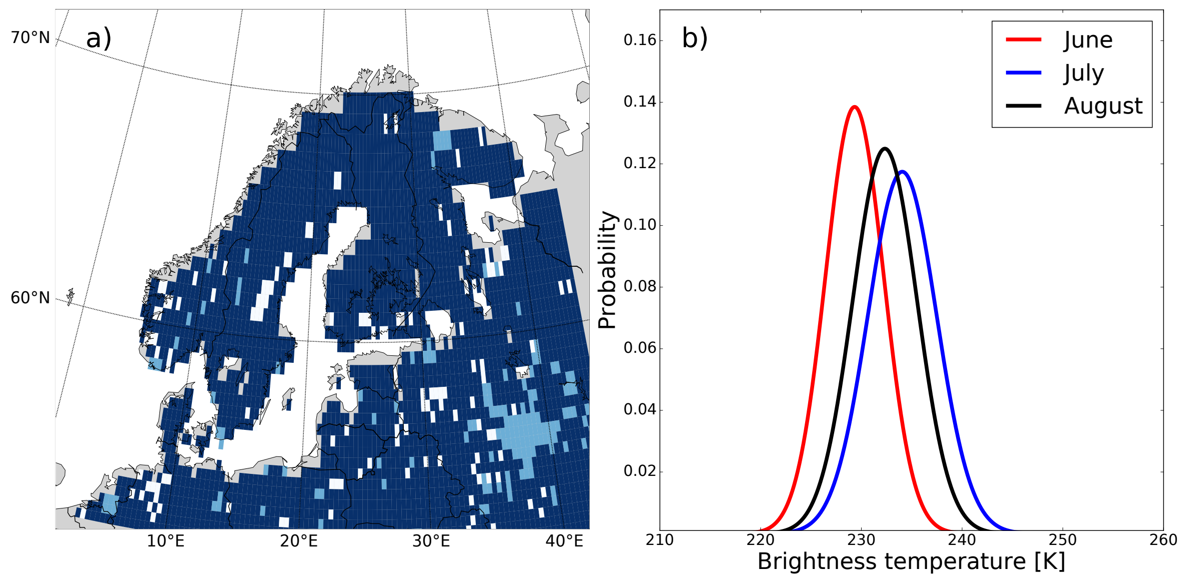

Figure 1. a) Shapiro-Wilk test for normality of the Tb_H distribution shown for July. Dark blue regions null-hypothesis is not rejected, i.e., the data appears to be normally distributed. Light blue regions null-hypothesis is rejected, and white regions (over land) had too few years of data for testing. **b)** PDFs of the fitted brightness temperature for boreal summmer months, June (red), July (blue) and August (black).

in Fig. 1 b). The distributions show that June has a lower mean Tb_H than July and August, with July being on average the warmest. The drought index value is computed by integrating the PDFs over $(0, Tb_H)$. The integral is approximated by a summation up to the Tb_H value of interest.

Preprints (www.preprints.org) | NOT PEER-REVIEWED | Posted: 1 April 2019 doi:10.20944/preprints201904.0009.v1

Peer-reviewed version available at Remote Sens. 2019, 11, 1200; doi:10.3390/rs11101200

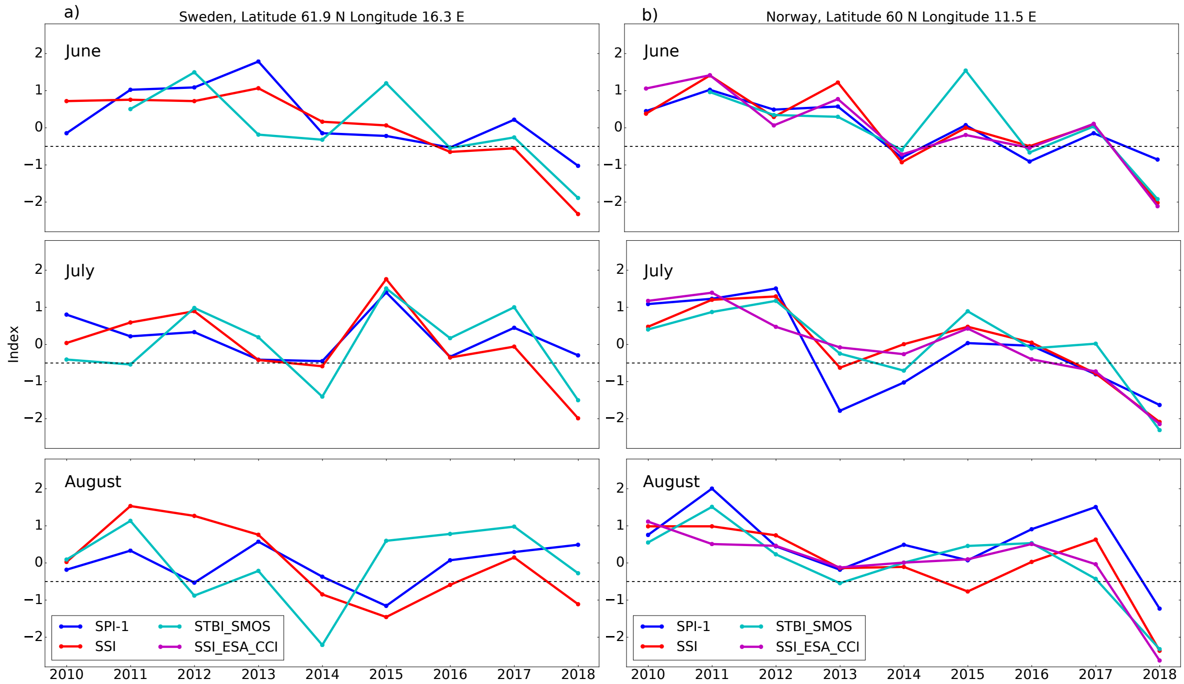

Figure 2. a) Time-series of the SPI-1 (blue), STBI_SMOS (cyan) and SSI_LDAS (red) over a grid-cell in Sweden (61.9° N and 16.3° E) from 2010 until 2018 for the boreal summer months June, July and August. The horizontal black dotted line indicate D0 drought conditions, see text for further explanation. Note that for this region there were no observations for the computation of the SSI_ESA_CCI. **b)** Same as a) but for a grid-cell in Norway (60.0° N and 11.5° E), here observations from the ESA CCI were available for the computation of the SSI_ESA_CCI drought index. For the different indices the grid-cell sizes are: 0.36° for the STBI_SMOS and 0.25° for the SPI-1, SSI_LDAS and SSI_ESA_CCI

3.1.2. Temporal and spatial patterns of the drought indices

Figure 2 shows time-series of the SPI-1 (blue), STBI_SMOS (cyan), SSI_LDAS (red) and SSI_ESA_CCI (mangenta) over a grid-cell in Sweden (61.9° N and 16.3° E) (a) and Norway (60.0° N and 11.5° E) (b) from 2010 until 2018 for the boreal summer months, June, July and August. The two regions were selected to represent a region with and without the SSI_ESA_CCI data, and therefore show how the STBI_SMOS can represent regions were soil moisture retrievals are masked. Furthermore, these two regions were affected by the 2018 summer drought, as seen from the negative anomalies in the indices for 2018. Depending on the severity, a drought can be classified into a drought scale or D-scale [2]. In this classification an SSI below 0.5 is defined as being abnormally dry. Using D0 as a drought threshold, we see that for the regions in Fig. 2 a) and b), severe drought conditions (see 2018 summer) is captured by the STBI_SMOS. The STBI_SMOS does not only capture dry events, it also captures years where a month is wetter than normal (index larger than zero). However, for positive index anomalies there seems to be more false events (e.g., June 2015 in Sweden, and June 2015 in Norway) than for the dry events. We evaluate how well the STBI_SMOS, SSI_ESA_CCI and SPI-1 could capture the temporal dynamics of the soil moisture drought by computing the correlation coefficients between the SSI_LDAS and the other metrics (STBI_SMOS, SSI_ESA_CCI and SPI-1). The LDAS-Monde index is then used as the reference index. This is justified by the fact that it incorporates both model and observation data in a data assimilation system. Other studies have shown that land data assimilation systems are able to correct for errors in precipitation datasets, and as a result, improve the representation of surface soil moisture (see for example Blyverket *et al.* [40]). Another example is provided by Albergel *et al.* [41], where the authors show that the LDAS-Monde improves the representation of the 2012 US corn belt drought. In the computation of the correlation coefficient, we used June, July and August (boreal summer) data together from 2011 until 2018 to increase the number of data-points. The domain average

Peer-reviewed version available at Remote Sens. 2019, 11, 1200; doi:10.3390/rs11101200

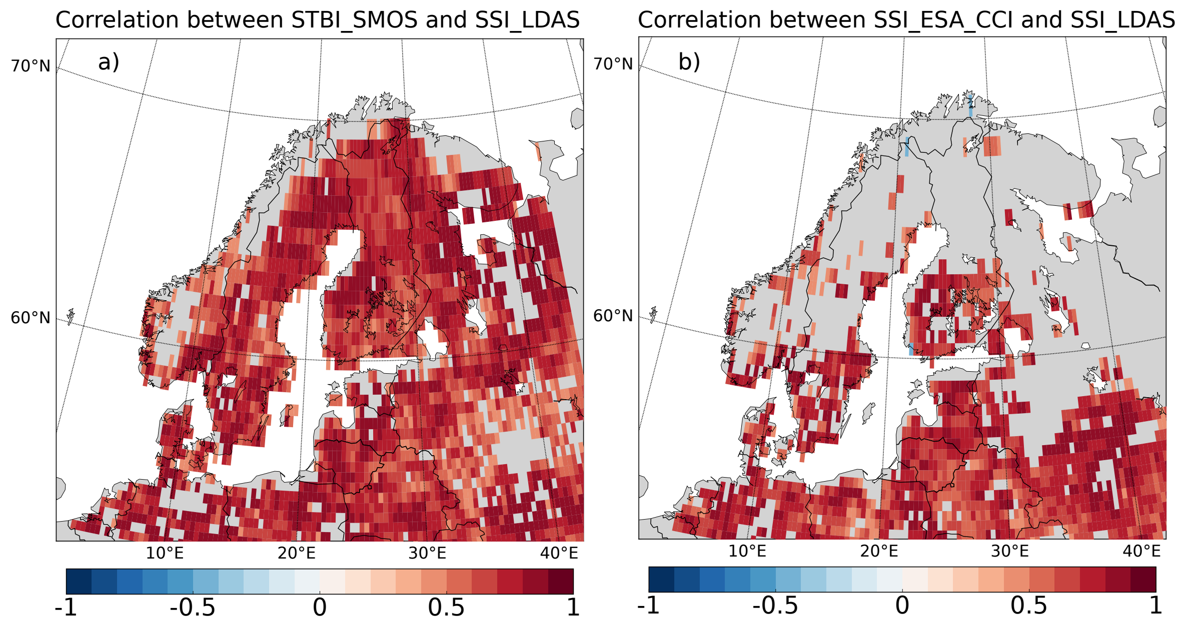

Figure 3. **a)** Pearson correlation coefficient between the STBI_SMOS and SSI_LDAS, red regions indicate a high positive correlation, masked (grey) regions have a correlation not significantly different from zero. **b)** Same as a) but for the Pearson correlation between the SSI_ESA_CCI and SSI_LDAS

was only computed for grid-cells where the Pearson correlation value was statistically significant at the 0.05 level. Figure 3 a) shows the Pearson correlation coefficient between the STBI_SMOS and SSI_LDAS, regions with no values (grey regions over land) had a correlation not different from zero at the 0.05 significance level. Most of the domain has a high correlation, except regions in south central Norway and from mid-Norway to northern Norway. In Fig. 3 b) the Pearson correlation coefficient between the SSI_ESA_CCI and SSI_LDAS is shown. Here large regions in the Nordic countries (Norway, Sweden and Finland) have non significant correlation. This is likely because the SSI_ESA_CCI index has large regions with missing data for the individual months, thus resulting in a non-significant correlation and discarded values (grey regions in Fig. 3). Summary statistics for the spatial correlations are shown in Table 1.

The STBI_SMOS has a correlation with the SSI_LDAS of 0.71, it also has the highest number of grid-cells with a statistically significant correlation value ($n = 2437$ out of 2997 grid-cells (81 %)). The SSI_ESA_CCI index had a correlation of 0.70 with the SSI_LDAS index, and significant values in $n = 1523$ out of 2997 (51 %) grid-cells. Finally, the SPI-1 correlation with SSI_LDAS was 0.56 for $n = 1537$ out of 2997 (51 %) grid-cells. The high correlation between the STBI_SMOS and the SSI_LDAS indicate that the STBI_SMOS is able to capture the variability in the soil moisture over the Nordic region as good as the SSI_ESA_CCI index. The number of grid-cells with statistically significant correlation values are higher for the STBI_SMOS than for the SSI_ESA_CCI, hence it provides better spatial coverage than the satellite derived soil moisture index. To check that the high-correlation is not only found in regions where the SSI_ESA_CCI data were missing, we also compute the correlation for grid-cells covered by both products, see Table 1. Here the mean correlation is only taken for grid-cells where we have data for all the four indices (resulting in 800 of 2997 land grid-cells being covered, i.e., 27 %).

3.2. *Summer 2018 Drought Case Study*

To further evaluate the performance of the STBI for drought mapping we utilized the 2018 summer drought over the Nordic countries as a case study.

Table 1. Pearson R correlation coefficient between the SSI_LDAS and the, STBI_SMOS, SSI_ESA_CCI and the SPI-1. Computed for individual grid-cells and summed over the whole domain (all columns) and over grid-cells with overlap between all datasets (overlap columns). *N* indicates grid-cells with statistically significant correlation at the 0.05 level, total number of land grid-cells were 2997.

	All		Overlap	
Index	R	N	R	N
STBI_SMOS	0.71	2437	0.70	800
SSI_ESA_CCI	0.70	1523	0.70	800
SPI-1	0.56	1537	0.56	800

3.2.1. Comparison between the STBI_SMOS, SSI_LDAS, SSI_ESA_CCI, SPI-1 and SSI_SMOS

The limited number of reliable satellite derived soil moisture observations in the SMOS-L2 (Fig. 4 q-t) and ESA CCI COMBINED product (Fig. 4 i-l) motivated our attempt to describe the 2018 Nordic drought using the observed brightness temperature (Tb_H). In addition to the poor coverage, the Standardized Soil moisture Index for SMOS (SSI_SMOS) exhibits noisy patterns, and little resemblance to the SSI_LDAS in Fig. 4. Comparing the STBI in Fig. 4 a-d) to the SSI_ESA_CCI in Fig. 4 i-l) we see that the STBI_SMOS has a better spatial coverage than the SSI_ESA_CCI. Large regions over Sweden and northern Finland are not covered by the SSI_ESA_CCI. This problem is addressed by using the Tb_H data.

Figures 4 a), e), i), m) and q) show the STBI_SMOS, SSI_LDAS, SSI_ESA_CCI, SPI-1 and SSI_SMOS over the Nordic region. The SPI-1 indicates a precipitation deficit for most of the domain. The STBI_SMOS, SSI_LDAS and SSI_ESA_CCI show that northern parts of Norway and the mountain regions in the south of Norway are wetter (colder for the STBI) than usual. This signal might come from late snowmelt wetting the soil in the northern latitudes and the mountainous regions in southern Norway. We also note that southern parts of Sweden and Finland are drier (warmer) than usual for the STBI_SMOS, SSI_LDAS and SSI_ESA_CCI. In general, the spatial patterns for May are very similar for the STBI and SSI_LDAS, although the STBI overestimates the wet regions in northern Norway and in Finland.

Next we examine the indices during June 2018. Figures 4 b), f), j), n) and r) show the STBI_SMOS, SSI_LDAS, SSI_ESA_CCI, SPI-1 and SSI_SMOS, respectively. The dry conditions seen in the SPI-1 continue in eastern Norway, southern Sweden and Denmark. Northern parts of Norway and most of Finland experience rainy conditions seen from the SPI-1. Eastern Norway, Sweden, Finland, Denmark and the Baltic countries have a dry anomaly in the STBI_SMOS, SSI_LDAS and SSI_ESA_CCI. Northern parts of Sweden and Finland have missing values for the SSI_ESA_CCI index; however, the STBI_SMOS shows similar patterns as the SSI_LDAS, except from the wet regions in southwestern and northern Norway. When comparing the STBI_SMOS to the SSI_LDAS we see that the STBI_SMOS captures the wet (cold) regions in the east of the domain.

For July in Figs. 4 c), g), k), o) and s) the SPI-1 shows a dry anomaly for Norway, Sweden, Finland and Denmark. In July, drought conditions were dominant over most of the domain, except for regions in the south central and east, which is reflected in all of the indices. Again, there are gaps in the SSI_ESA_CCI over large regions of Sweden and Finland. These gaps are not present in the STBI_SMOS, which is consistent with the SSI_LDAS, showing dry anomalies for this region. Close to normal conditions in northern parts of Poland are found for both the STBI_SMOS and the SSI_LDAS for July; this is not seen for the SSI_ESA_CCI.

For August most of Norway experienced wetter than usual conditions (seen from the SPI-1), this is reflected in the SSI_ESA_CCI and the SSI_LDAS, but not in the STBI_SMOS, see Figs. 4 d), h), l) and p). One reason for this could be precipitation intercepted by the vegetation, increasing the VWC, again

Preprints (www.preprints.org) | NOT PEER-REVIEWED | Posted: 1 April 2019 doi:10.20944/preprints201904.0009.v1

Peer-reviewed version available at Remote Sens. 2019, 11, 1200; doi:10.3390/rs11101200

increasing the emissivity from the vegetation. Higher emissivity for wetter vegetation could therefore mask out precipitation events and cause a false drought signal for this month.

3.2.2. Drought Severity

Following the D-scale [2], an SSI below −1.3 is defined as a severe drought (D2 conditions). In Fig. 5 we have plotted the STBI_SMOS (a-d), SSI_LDAS (e-h), SSI_ESA_CCI (i-l) and SPI-1 (m-p) for D2 conditions for May, June, July and August in 2018. The difference between the one-month land surface indices (STBI_SMOS, SSI_LDAS and SSI_ESA_CCI) and the SPI-1 is most likely due to the lag time between the meteorological drought (one-month SPI) and the agricultural drought (one-month SSI). The SPI-1 has a shorter memory than the SSI, hence a dry SPI-1 in month i is often followed by a dry SSI in month $i+1$, even though the precipitation is back to normal conditions in month $i+1$. Using the SSI_LDAS as a reference we see that the STBI_SMOS is able to capture regions in severe drought where the SSI_ESA_CCI has masked values from the retrieval. This can be seen in southern Norway (July) and northern and central Sweden (July). Comparing Figs. 5 c), g) and k) we see that northern parts of Poland do not have severe drought conditions for the SSI_LDAS, and this is captured by the STBI_SMOS but not by the SSI_ESA_CCI. On the other hand, the spatial pattern of the SSI_ESA_CCI drought severity in June has better agreement with the SSI_LDAS than the comparison of the STBI_SMOS versus the SSI_LDAS. In August the STBI_SMOS (Fig. 2 d)) is overestimating the regions experiencing severe drought conditions in northern Norway and Sweden, when compared to the SSI_LDAS (Fig. 5 h)).

3.2.3. Drought Onset and Recovery

Accurate monitoring of drought onset and recovery could help farmers and decision makers minimize the negative impacts of a drought. Here we evaluate the temporal evolution of the STBI_SMOS index against the temporal evolution of the SSI_LDAS SSI_ESA_CCI and SPI-1 during the 2018 summer drought. As a consequence of the drought several regions in the Nordic countries experienced wildfires and agricultural losses [7,42], here we have chosen three sites to represent such conditions. In Fig. 6 we have selected grid-cells in the vicinity of a) Jokkmokk municipality, Sweden, b) Tovaasen, Sweden and c) Nes in Akershus municipality, Norway. These regions experienced large wildfires and agricultural droughts during the summer 2018 heatwave. The horizontal dotted black line shows the D0 condition (moderate drought). The first thing to note is that in Fig. 6 a) and b) there are no data for the SSI_ESA because these grid locations are flagged in the retrieval algorithm. This limits the use of the SSI_ESA_CCI over regions in the Nordic countries for drought monitoring and mapping. Hence a reason for choosing grid-cells where we have no SSI_ESA_CCI data is to show that the STBI_SMOS can be used to monitor the drought in these regions.

Jokkmokk municipality lies above the Arctic circle in northern Sweden and it experienced large wildfires during the 2018 summer. In Fig. 6 a) we see that the precipitation deficit (low SPI-1) starting in May causes the STBI_SMOS (cyan) and SSI_LDAS (red) to fall below D0 conditions in June. The close to normal SPI-1 conditions in June has little impact on the land surface indices (STBI_SMOS and SSI_LDAS). Precipitation deficit in July and only close to normal SPI-1 conditions in August and September, results in a slow recovery of the land surface indices for the Jokkmokk site.

Tovaasen lies in the Ljusdalen muncipality, a region in Sweden which experienced large wildfires in mid-July 2018. In Fig. 6 b) we see that the SPI-1 (blue) is close to normal for February, March and April. In May and June the precipitation deficit leads to a decrease in the STBI_SMOS (cyan) and SSI_LDAS (red). In August the SPI-1 is close to normal conditions, but this is not enough for the STBI_SMOS and SSI_LDAS to recover. In September the STBI_SMOS and the SSI_LDAS diverges, with the STBI_SMOS showing drought recovery while the SSI_LDAS more closely follows the SPI-1 and shows drought conditions.

Much of the agriculture in Norway lies in the south-eastern parts of the country and here we choose a grid-cell which covers Nes in Akershus municipality. In Fig. 6 c) we see that low SPI-1 conditions in the February and March likely caused abnormally dry (warm) conditions in April for the STBI_SMOS (cyan) and SSI_ESA_CCI (magenta). The continued precipitation deficit in May, June and July was propagated into the land seen by the low STBI_SMOS, SSI_LDAS and SSI_ESA_CCI. Here the three land surface drough indices follow each other closely during the dry spell in May, June, July and August.

The summer 2018 case study show that the STBI_SMOS has potential to supplement information to drought monitoring over the Nordic region. Especially, we see that it was able to monitor the drought in regions where data from the soil moisture retrievals were missing. The STBI_SMOS did however miss the transition to a wet anomaly for large regions in Norway in August 2018 (Fig. 4 d)).

4. Conclusions

In this study we outlined a new approach for directly applying passive microwave brightness temperature to monitor and map drought over the Nordic countries. We propose a standardized index (STBI) based on passive microwave brightness temperature data (Tb_H). The rationale behind this choice is that the Tb_H convolves information about soil moisture, soil temperature and vegetation water content, which are all important factors in drought monitoring. The brightness temperature also provides a better spatial and temporal coverage than the retrieved soil moisture, because we avoid the retrieval problem, which is problematic over northern latitudes owing to dense vegetation, strong topography, high water fraction and snow cover. The brightness temperature is also available earlier than than the retrieved soil moisture, which will benefit the drought monitoring capabilities of the index.

We found that the STBI_SMOS metric was able to capture the spatial patterns of the drought, especially for the very dry conditions seen in July 2018, when comparing it to the SSI from LDAS-Monde. As seen for two test sites in Sweden and one in Norway, the STBI_SMOS drought onset and end were in line with the SSI_LDAS and SPI-1. The STBI_SMOS was also characterized by a one-month lag compared to the SPI-1 (as often seen in land surface drought metrics [37]), indicating that it contained information about soil/vegetation moisture, and not only about land surface temperature.

The results from this work show that observations from passive microwave observations (in the L-band) could be implemented in a Nordic drought monitoring system. We expect that the STBI could be a supplement to modelling tools, and that downscaling of the index would enhance its applicability for drought monitoring at decision making scales. In the future it would be possible to calculate the STBI for observations from more recently launched L-band satellites, such as the Soil Moisture Active Passive (SMAP) NASA mission [19]. The performance of passive microwave observations in the C-band should also be investigated for drought monitoring over northern latitudes because the temporal span of these missions are longer than the L-band missions, and hence a more reliable estimate of the (Tb_H) climatology can be computed. The method could also be expanded to other regions of the world, where retrieval of soil moisture is difficult. This study was also the first attempt to monitor agricultural drought over this region from space and compare the skill of a space based drought index with that of a state-of-the-art land surface data assimilation system (LDAS-Monde). We expect that future development of the STBI_SMOS metric could benefit farmers, decision makers and others depending on information concerning agricultural drought over the Nordic countries.

Author Contributions: JB, PDH WAL, CA and PS conceived and designed the study. CA designed and ran the land surface data assimilation system. JB did the analysis and wrote the manuscript. All authors provided comments on the manuscript.

Funding: The main author is supported by the Research Council of Norway (NFR PhD-grant 239947, 2015-2018)

Acknowledgments: The main author would like to thank Laurent Bertino for helpful comments in the preparation of this paper. The authors would like to thank the Copernicus Global Land Service for providing the satellite-derived LAI products and soil moisture for the LDAS-Monde assimilation. We would also like to thank the Copernicus Climate Change Service (C3S) for providing the ESA CCI COMBINED soil moisture data, and the ERA-5 data used for atmospheric forcing in the LDAS-Monde system. We acknowledge the E-OBS dataset from the EU-FP6 project ENSEMBLES (http://ensembles-eu.metoffice.com) and the data providers in the ECAD

project (http://www.ecad.eu). The SMOS data are available online from ESA. The Copernicus Climate Change soil moisture data are available at https://cds.climate.copernicus.eu. The LDAS-Monde derived data and analysis scripts can be accessed at ftp://ftp.nilu.no/Pub/nilu/jostein/Data/, this will be updated to Zenodo and Github at a later stage.

Conflicts of Interest: The authors declare no conflict of interest.

1. Gerber, N.; Mirzabaev, A. Benefits of action and costs of inaction: Drought mitigation and preparedness – a literature review. Technical report, World Meteorological Organization (WMO) and Global Water Partnership (GWP), 2017.
2. Svoboda, M. Drought Monitor. *Bulletin of the American Meteorological Society* **2002**, pp. 1181–1190. doi:10.1175/1520-0477(2002)083<1181:TDM>2.3.CO;2.
3. Luo, L.; Wood, E.F. Monitoring and predicting the 2007 U.S. drought. *Geophysical Research Letters* **2007**, *34*. doi:10.1029/2007GL031673.
4. Lentze, G. Newsletter No. 157 - Autumn 2018. *ECMWF Newsletter* **2018**.
5. WMO. The State of the Global Climate in 2018. Technical report, 2018.
6. Landbruksdirektoratet. *Landbruksdirektoratet*. Available at https://www.landbruksdirektoratet.no/no/statistikk/landbrukserstatning/klimarelaterte-skader-og-tap/avlingssvikt, Accessed: 28 March 2019.
7. Skaland, R.G.; Colleuille, H.; Andersen, A.S.H.; Mamen, J.; Grinde, L.; Tajet, H.T.T.; others. Tørkesommeren 2018. Technical report, The Norwegian Meteorological Institute, Oslo, 2019.
8. Samaniego, L.; Thober, S.; Kumar, R.; Wanders, N.; Rakovec, O.; Pan, M.; others. Anthropogenic warming exacerbates European soil moisture droughts. *Nature Climate Change* **2018**, *8*, 421–426. doi:10.1038/s41558-018-0138-5.
9. Trenberth, K.E.; Dai, A.; Van Der Schrier, G.; Jones, P.D.; Barichivich, J.; Briffa, K.R.; Sheffield, J. Global warming and changes in drought, 2014, [arXiv:1011.1669v3]. doi:10.1038/nclimate2067.
10. Mu, Q.; Zhao, M.; Kimball, J.S.; McDowell, N.G.; Running, S.W. A remotely sensed global terrestrial drought severity index. *Bulletin of the American Meteorological Society* **2013**, *94*, 83–98. doi:10.1175/BAMS-D-11-00213.1.
11. AghaKouchak, A.; Farahmand, A.; Melton, F.S.; Teixeira, J.; Anderson, M.C.; Wardlow, B.D.; Hain, C.R. Remote sensing of drought: Progress, challenges and opportunities, 2015. doi:10.1002/2014RG000456.
12. Sadri, S.; Wood, E.F.; Pan, M. Developing a drought-monitoring index for the contiguous US using SMAP. *Hydrology and Earth System Sciences* **2018**, *22*, 6611–6626. doi:10.5194/hess-22-6611-2018.
13. Kerr, Y.H.; Waldteufel, P.; Richaume, P.; Wigneron, J.P.; Ferrazzoli, P.; Mahmoodi, A.; others. The SMOS soil moisture retrieval algorithm. *IEEE Transactions on Geoscience and Remote Sensing* **2012**, *50*, 1384–1403. doi:10.1109/TGRS.2012.2184548.
14. Fernandez-Moran, R.; Al-Yaari, A.; Mialon, A.; Mahmoodi, A.; Al Bitar, A.; De Lannoy, G.; others. SMOS-IC: An alternative SMOS soil moisture and vegetation optical depth product. *Remote Sensing* **2017**, *9*. doi:10.3390/rs9050457.
15. Jones, A.S.; Vukićević, T.; Vonder Haar, T.H. A Microwave Satellite Observational Operator for Variational Data Assimilation of Soil Moisture. *Journal of Hydrometeorology* **2004**, *5*, 213–229, [1511.04103]. doi:10.1175/1525-7541(2004)005<0213:AMSOOF>2.0.CO;2.
16. ESA. ESA SMOS Online Dissemination Service.
17. Wigneron, J.P.; Kerr, Y.; Waldteufel, P.; Saleh, K.; Escorihuela, M.J.; Richaume, P.; Ferrazzoli, P.; de Rosnay, P.; Gurney, R.; Calvet, J.C.; Grant, J.P.; Guglielmetti, M.; Hornbuckle, B.; Mätzler, C.; Pellarin, T.; Schwank, M. L-band Microwave Emission of the Biosphere (L-MEB) Model: Description and calibration against experimental data sets over crop fields. *Remote Sensing of Environment* **2007**, *107*, 639–655. doi:10.1016/j.rse.2006.10.014.
18. Njoku, E.G.; Wilson, W.J.; Yueh, S.H.; Dinardo, S.J.; Li, F.K.; Jackson, T.J.; others. Observations of soil moisture using a passive and active low-frequency microwave airborne sensor during SGP99. *IEEE Transactions on Geoscience and Remote Sensing* **2002**, *40*, 2659–2673. doi:10.1109/TGRS.2002.807008.

19. Entekhabi, D.; Njoku, E.G.; O'Neill, P.E.; Kellogg, K.H.; Crow, W.T.; Edelstein, W.N.; others. The soil moisture active passive (SMAP) mission. *Proceedings of the IEEE* **2010**, *98*, 704–716. doi:10.1109/JPROC.2010.2043918.
20. De Rosnay, P.; Drusch, M.; Boone, A.; Balsamo, G.; Decharme, B.; Harris, P.; others. AMMA land surface model intercomparison experiment coupled to the community microwave emission model: ALMIP-MEM. *Journal of Geophysical Research Atmospheres* **2009**, *114*. doi:10.1029/2008JD010724.
21. Drusch, M.; Holmes, T.; de Rosnay, P.; Balsamo, G. Comparing ERA-40-Based L-Band Brightness Temperatures with Skylab Observations: A Calibration/Validation Study Using the Community Microwave Emission Model. *Journal of Hydrometeorology* **2009**, *10*, 213–226. doi:10.1175/2008JHM964.1.
22. De Lannoy, G.J.; Reichle, R.H. Assimilation of SMOS brightness temperatures or soil moisture retrievals into a land surface model. *Hydrology and Earth System Sciences* **2016**, *20*, 4895–4911. doi:10.5194/hess-20-4895-2016.
23. Dorigo, W.; Gruber, A.; De Jeu, R.A.; Wagner, W.; Stacke, T.; Loew, A.; others. Evaluation of the ESA CCI soil moisture product using ground-based observations. *Remote Sensing of Environment* **2015**, *162*, 380–395. doi:10.1016/j.rse.2014.07.023.
24. Dorigo, W.; Wagner, W.; Albergel, C.; Albrecht, F.; Balsamo, G.; Brocca, L.; others. ESA CCI Soil Moisture for improved Earth system understanding: State-of-the art and future directions. *Remote Sensing of Environment* **2017**, *203*, 185–215. doi:10.1016/j.rse.2017.07.001.
25. Scanlon, T.; Chung, D.; Paulik, C.; Kidd, R. Product User Guide and Specification. Technical report, 2018.
26. Haylock, M.R.; N. Hofstra.; A.M.G. Klein Tank.; E.J. Klok.; P.D. Jones.; New., M. A European daily high-resolution gridded dataset of surface temperature and precipitation. *Journal of Geophysical Research-Atmospheres* **2008**, *113*, D20119, [1201.1509]. doi:10.1029/2008JD010201.
27. Albergel, C.; Munier, S.; Jennifer Leroux, D.; Dewaele, H.; Fairbairn, D.; Lavinia Barbu, A.; others. Sequential assimilation of satellite-derived vegetation and soil moisture products using SURFEX-v8.0: LDAS-Monde assessment over the Euro-Mediterranean area. *Geoscientific Model Development* **2017**, *10*, 3889–3912. doi:10.5194/gmd-10-3889-2017.
28. Albergel, C.; Dutra, E.; Bonan, B.; Zheng, Y.; Munier, S.; Balsamo, G.; de Rosnay, P.; Muñoz-Sabater, J.; Calvet, J.C. Monitoring and Forecasting the Impact of the 2018 Summer Heatwave on Vegetation. *Remote Sensing* **2019**, *11*. doi:https://doi.org/10.3390/rs11050520.
29. Noilhan, J.; Mahfouf, J.F. The ISBA land surface parameterisation scheme. *Global and Planetary Change* **1996**, *13*, 145–159. doi:10.1016/0921-8181(95)00043-7.
30. Calvet, J.C.; Noilhan, J.; Roujean, J.L.; Bessemoulin, P.; Cabelguenne, M.; Olioso, A.; Wigneron, J.P. An interactive vegetation SVAT model tested against data from six contrasting sites. *Agricultural and Forest Meteorology* **1998**, *92*, 73–95. doi:10.1016/S0168-1923(98)00091-4.
31. Masson, V.; Le Moigne, P.; Martin, E.; Faroux, S.; Alias, A.; Alkama, R.; others. The SURFEXv7.2 land and ocean surface platform for coupled or offline simulation of earth surface variables and fluxes. *Geoscientific Model Development* **2013**, *6*, 929–960. doi:10.5194/gmd-6-929-2013.
32. Mahfouf, J.F.; Bergaoui, K.; Draper, C.; Bouyssel, F.; Taillefer, F.; Taseva, L. A comparison of two off-line soil analysis schemes for assimilation of screen level observations. *Journal of Geophysical Research Atmospheres* **2009**, *114*. doi:10.1029/2008JD011077.
33. Albergel, C.; Calvet, J.C.; Mahfouf, J.F.; Rüdiger, C.; Barbu, A.L.; Lafont, S.; others. Monitoring of water and carbon fluxes using a land data assimilation system: A case study for southwestern France. *Hydrology and Earth System Sciences* **2010**, *14*, 1109–1124. doi:10.5194/hess-14-1109-2010.
34. Barbu, A.L.; Calvet, J.C.; Mahfouf, J.F.; Albergel, C.; Lafont, S. Assimilation of Soil Wetness Index and Leaf Area Index into the ISBA-A-gs land surface model: Grassland case study. *Biogeosciences* **2011**, *8*, 1971–1986. doi:10.5194/bg-8-1971-2011.
35. De Rosnay, P.; Drusch, M.; Vasiljevic, D.; Balsamo, G.; Albergel, C.; Isaksen, L. A simplified extended kalman filter for the global operational soil moisture analysis at ECMWF. *Quarterly Journal of the Royal Meteorological Society* **2013**, *139*, 1199–1213. doi:10.1002/qj.2023.
36. Farahmand, A.; AghaKouchak, A.; Teixeira, J. A vantage from space can detect earlier drought onset: An approach using relative humidity. *Scientific Reports* **2015**, *5*. doi:10.1038/srep08553.
37. Sheffield, J.; Goteti, G.; Wen, F.; Wood, E.F. A simulated soil moisture based drought analysis for the United States. *Journal of Geophysical Research D: Atmospheres* **2004**, *109*, 1–19. doi:10.1029/2004JD005182.

Peer-reviewed version available at *Remote Sens.* **2019**, *11*, 1200; doi:10.3390/rs11101200

38. Gringorten, I.I. A plotting rule for extreme probability paper. *Journal of Geophysical Research* **1963**, *68*, 813–814. doi:10.1029/JZ068i003p00813.
39. Wilks, D.S. *Statistical methods in atmospheric sciences*; Vol. 100, 2005; p. 676. doi:10.1198/jasa.2007.s163.
40. Blyverket, J.; Hamer, P.D.; Bertino, L.; Albergel, C.; Fairbairn, D.; Lahoz, W.A. An Evaluation of the EnKF vs. EnOI and the Assimilation of SMAP, SMOS and ESA CCI Soil Moisture Data over the Contiguous US. *Remote Sensing* **2019**, *11*. doi:10.3390/rs11050478.
41. Albergel, C.; Munier, S.; Bocher, A.; Bonan, B.; Zheng, Y.; Draper, C.; Leroux, D.J.; Calvet, J.C. LDAS-Monde sequential assimilation of satellite derived observations applied to the contiguous US: An ERA-5 driven reanalysis of the land surface variables. *Remote Sensing* **2018**, *10*. doi:10.3390/rs10101627.
42. Watts, J. The Swedish town on the frontline of the Arctic wildfires. https://www.theguardian.com/world/2018/jul/30/the-swedish-town-on-the-frontline-of-the-arctic-wildfires, 2018. Accessed: 2019-02-07.

Peer-reviewed version available at *Remote Sens.* **2019**, *11*, 1200; doi:10.3390/rs11101200

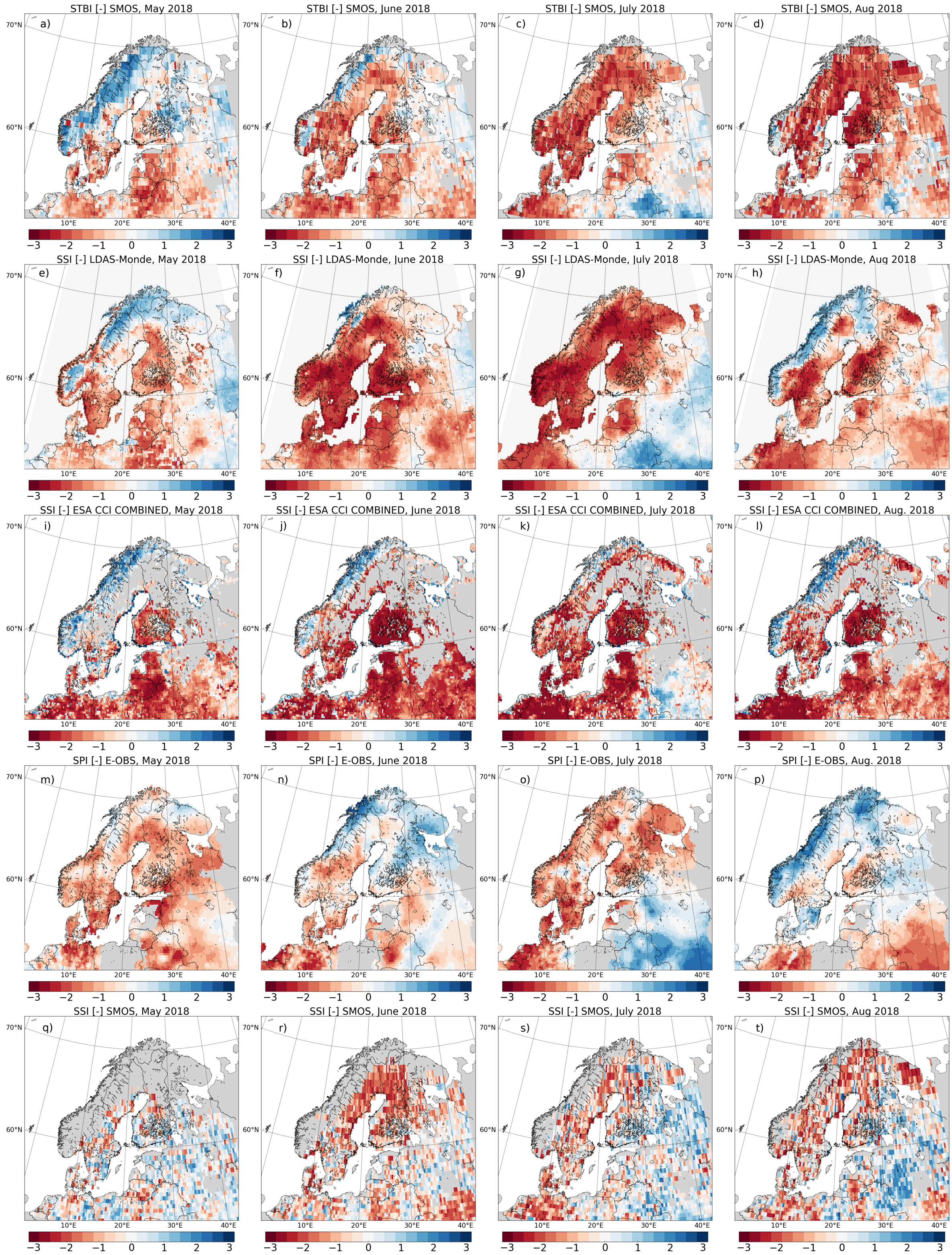

Figure 4. Drought indices, blue/red is above/below average precipitation, Tb_H or soil moisture. Grey colour indicates regions without data. Columns from left to right are for May, June, July and August. **(a-d)** Standardized microwave Brightness Temperature Index (STBI_SMOS). **(e-h)** Standardized Soil moisture Index (SSI_LDAS). **(i-l)** Standardized Soil moisture Index ESA CCI (SSI_ESA_CCI). **(m-p)** Standardized Precipitation Index (SPI-1). **(q-t)** Standardized Soil moisture Index SMOS (SSI_SMOS).

Preprints (www.preprints.org) | NOT PEER-REVIEWED | Posted: 1 April 2019 doi:10.20944/preprints201904.0009.v1

Peer-reviewed version available at Remote Sens. 2019, 11, 1200; doi:10.3390/rs11101200

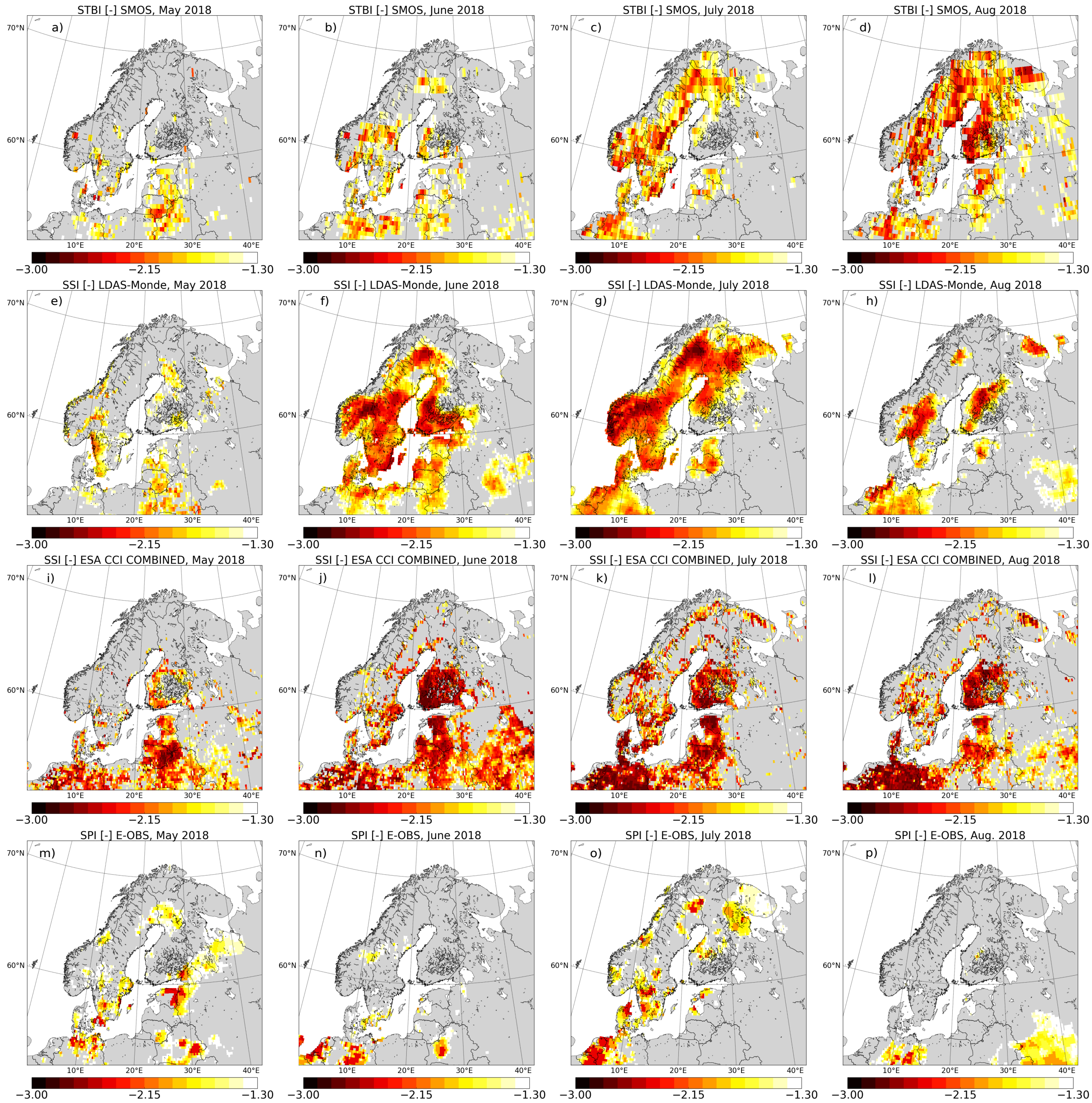

Figure 5. Regions with severe drought conditions, drought index < -1.3 for May, June, July and August. Red regions are severe drought conditions, while yellow and white are regions with less severe drought conditions. Grey colour indicates regions where the drought indices are larger than -1.3. **(a-d)** STBI < -1.3. **(e-h)** SSI_LDAS < -1.3. **(i-l)** SSI_ESA_CCI < -1.3. **(m-p)** SPI-1 < -1.3.

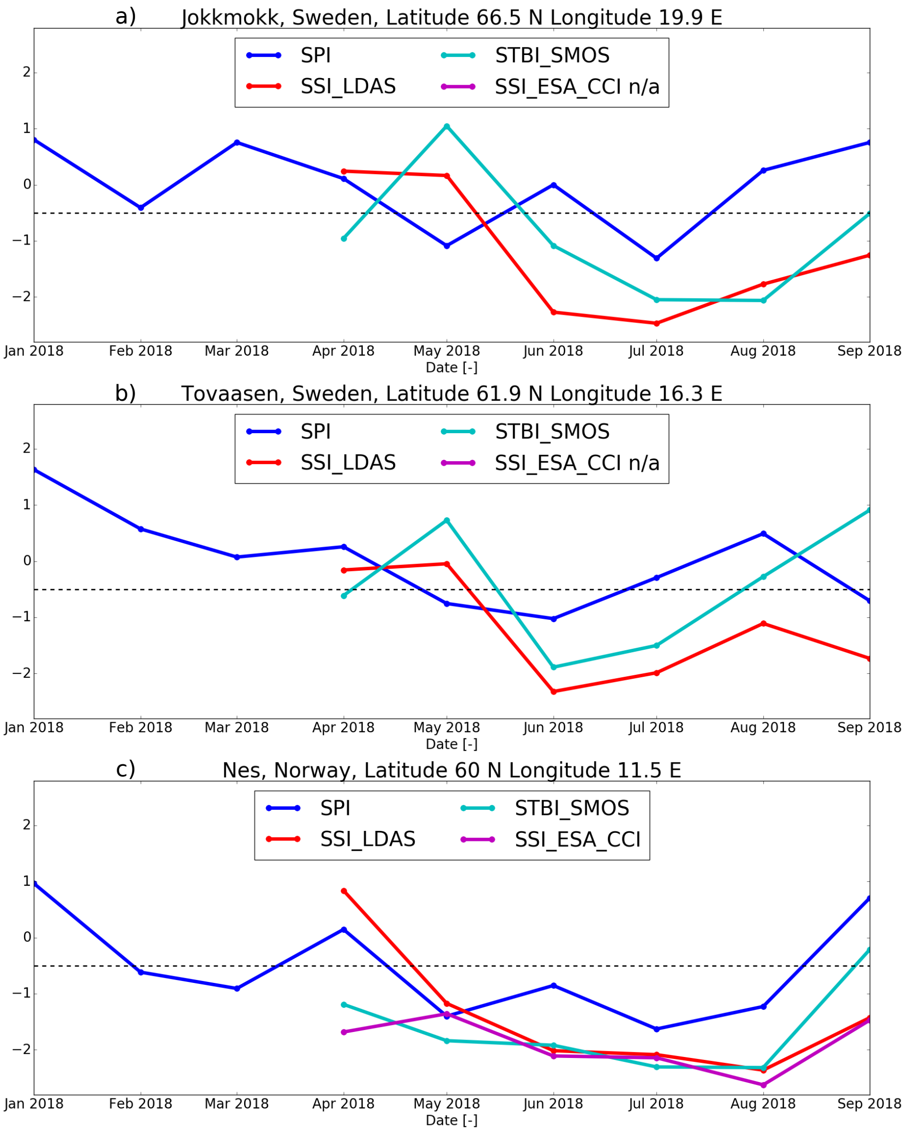

Figure 6. SPI-1 (blue), SSI_LDAS (red), STBI_SMOS (cyan) and SSI_ESA_CCI (magenta) time series.Black dotted horizontal line indicate D0 drought conditions. **a)** Jokkmokk municipality, Sweden, **b)** Tovaasen, Sweden, **c)** Nes in Akershus municipality, Norway. Latitudes are given in degrees north (N) and longitudes are given in degrees east (E)